Photothermal treatment of prostate tumor with micellar indocyanine green and Napabucasin to co-ablate cancer cells and cancer stem cells

Yanyi Qu, Beibei Guo, Songsong Zhao, Juan Sun, Jun Cao, Mingyu Xia, Zhiyuan Zhong, Fenghua Meng

PII: S0168-3659(25)00324-4

DOI: https://doi.org/10.1016/j.jconrel.2025.113704

Reference: COREL 113704

To appear in: *Journal of Controlled Release*

Received date: 28 December 2024

Revised date: 2 April 2025

Accepted date: 4 April 2025

Please cite this article as: Y. Qu, B. Guo, S. Zhao, et al., Photothermal treatment of prostate tumor with micellar indocyanine green and Napabucasin to co-ablate cancer cells and cancer stem cells, *Journal of Controlled Release* (2024), https://doi.org/10.1016/j.jconrel.2025.113704

Photothermal Treatment of Prostate Tumor with Micellar Indocyanine Green and Napabucasin to Co-ablate Cancer Cells and Cancer Stem Cells

Yanyi Qu[a], Beibei Guo[a], Songsong Zhao[a], Juan Sun[a], Jun Cao[a], Mingyu Xia[a], Zhiyuan Zhong[a,b,]*, Fenghua Meng[a,]*

[a] *Biomedical Polymers Laboratory, College of Chemistry, Chemical Engineering and Materials Science, and State Key Laboratory of Radiation Medicine and Protection, Soochow University, Suzhou, 215123, P. R. China*

[b] *College of Pharmaceutical Sciences, Soochow University, Suzhou, 215123, P. R. China*

* Corresponding authors.

Tel/Fax: +86-512-65880098, Email: zyzhong@suda.edu.cn (Z. Zhong);

Tel/Fax: +86-512-65882060, Email: fhmeng@suda.edu.cn (F. Meng).

Abstract

Advanced prostate cancer is hassled by relapse and metastasis that are closely associated with cancer stem cells (CSCs). Here, we present micellar indocyanine green and napabucasin (mICG-Nap) that co-ablates cancer cells and CSCs via photothermal therapy (PTT) for the treatment of prostate tumor. mICG-Nap with stable loading of both drugs and favorable size effectively reduced CSC population in RM1-PSMA murine prostate cancer cells and inhibited tumor spheroid formation. mICG-Nap showed an enhanced photothermal effect compared with free ICG and eliminated tumor spheroids under near-infrared (NIR) irradiation. The efficacy of mICG-Nap was further enhanced by decorating with Acupa ligand, which targets to RM1-PSMA cells and tumors via PSMA receptor. The enhanced tumor cell uptake of Acupa-mICG-Nap led to significant survival benefits in both subcutaneous RM1-PSMA tumor models and postoperative models. The tumor analyses demonstrated clear downregulation of CSC-related biomarkers such as OCT4, SOX2, CD133 and pSTAT3 as well as PSMA by Acupa-mICG-Nap. Rational formulated micellar indocyanine green and napabucasin plus NIR appears as an appealing strategy to co-ablate cancer cells and CSCs with rapid tumor de-bulking yet no recurrence.

Keywords: Micelles; Photothermal therapy; Cancer stem cells; Prostate cancer; Targeted delivery

1. Introduction

Prostate cancer is a top life-threatening malignancy for men worldwide [1, 2]. The existing therapies such as androgen deprivation therapy, chemotherapy and radiotherapy while effective for prostate cancer patients diagnosed at an early stage are unable to alleviate advanced cases [2, 3]. One major issue with advanced prostate cancer is hard to eliminate cancer stem cells (CSCs) that play a vital role in tumor relapse and metastasis [4-6]. CSCs are a small but fatal subset of the tumor population, characterized by their strong self-renewal capacity and differentiation potential [7]. CSCs reside in the hypoxic niches and exist in a quiescent state, allowing them to evade conventional therapies and contributing to treatment resistance, tumor recurrence and metastasis. As a matter of fact, CSCs proportion is typically subject to a big increase after most treatments [5].

In the past decade, different strategies e.g. targeting ATP-binding cassette transporters, DNA damage repair mechanisms, autophage, ferroptosis and immunosuppression have been explored to inhibit the CSCs in prostate cancer [8, 9]. The leverage of CSC pathways, such as Hedgehog, STAT3, Wnt, Notch and NF-kB, has led to the development of differentiators and inhibitors, some of which have progressed to clinical trials [10, 11]. Notably, the over-activation of STAT3 pathway is implicated in prostate cancer pathogenesis and correlates with poor patient prognosis [12], as also evidenced by elevated levels of IL-6, IL-6 receptor, JAK1, and pSTAT3 in advanced prostate cancer patients [13]. The small molecular STAT3 inhibitor napabucasin (Nap) has demonstrated potential in inhibiting CSCs across various solid tumors including prostate cancer [14, 15]. Its therapeutic efficacy has been evaluated in monotherapy and combination therapies (pembrolizumab, paclitaxel, nab-paclitaxel, gemcitabine, or FOLFIRI) in clinical trials for several types of metastatic tumors [16-19]. It should be noted, however, that despite certain progress, few systems have been developed to simultaneously eliminate bulk tumor and CSCs [20, 21].

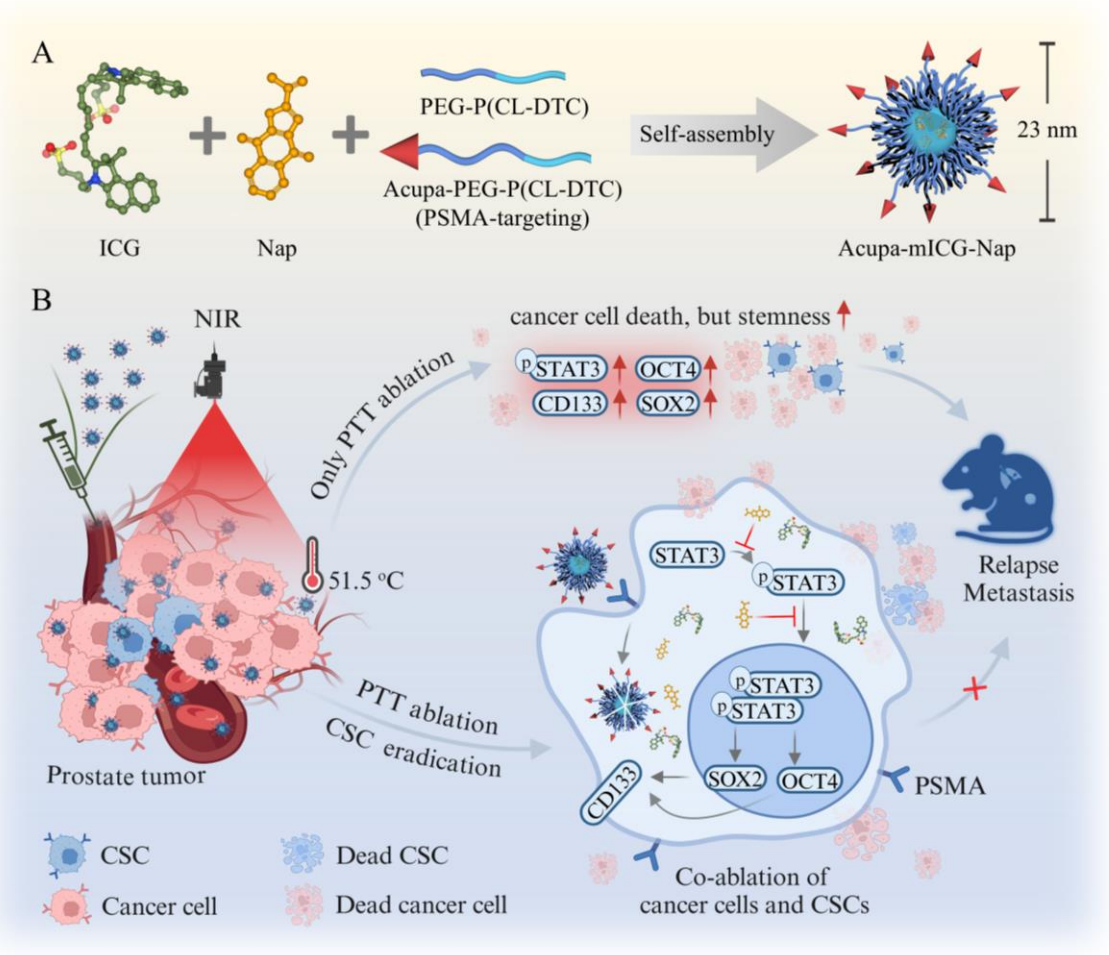

Scheme 1. Schematic illustration of (A) the facile fabrication of Acupa-mICG-Nap, and (B) combination strategy of PTT ablation with CSC eradication to prevent prostate cancer relapse and metastasis. The figure was created using BioRender.

Here, we report on micellar indocyanine green and napabucasin (mICG-Nap) plus near-infrared (NIR) irradiation to co-ablate cancer cells and CSCs, via photothermal therapy (PTT) and CSC elimination for effective treatment of prostate cancer (Scheme 1). PTT enables rapid tumor debulking in various tumor models by localized heating (48-60 ℃) [22, 23]. ICG was selected as a photosensitizer due to its strong PTT properties and FDA approval. But ICG is associated with fast clearance and lacks targeting ability [24], and PTT monotherapy often leads to swift tumor relapse and metastasis [25]. Nap, compared to conventional anticancer drugs, exhibits capacity to inhibit both tumor cells and CSCs with favourable safety profiles, making it an ideal candidate for combination therapy with PTT

ablation. However, Nap failed to yield satisfactory outcomes in phase III clinical trial, attributable to the low bioavailability stemming from its highly crystalline and lipophilic structure that also poses great challenges in formulation. Only recently, there are limited success in developing Nap nanoformulations [26-28]. Interestingly, we found that disulfide-crosslinked biodegradable micelles based on poly(ethylene glycol)-*b*-poly(ε-caprolactone-*co*-dithiolane trimethylene carbonate) (PEG-P(CL-DTC) could efficiently and stably coload ICG and Nap. This micellar nanodrug strategy not only enables successful nanoformulation of Nap and ICG but also facilitates efficient PTT ablation and CSC eradication. The micelles based on PEG-P(CL-DTC) have been employed for the targeted delivery of paclitaxel, docetaxel and gemcitabine [29-31]. mICG-Nap was further decorated with an Acupa ligand (Acupa-mICG-Nap), which targets to RM1-PSMA prostate cancer cells and tumors via binding with PSMA [32, 33]. Lutetium-177-PSMA-617 has been approved by FDA for the treatment of metastatic castration-resistant prostate cancer patients [34, 35]. Of note, our results showed that Acupa-mICG-Nap in combination with NIR irradiation resulted in significant survival benefits in both subcutaneous RM1-PSMA tumor models and postoperative models, by simultaneously alleviating prostate cancer cells and CSCs.

2. Experimental section

2.1. Preparation and characterizations of mICG-Nap and Acupa-mICG-Nap

ICG and Nap were mixed at various molar ratios (0.75:1, 1:1, 1.5:1, and 2:1) in PEG350. The mixture was added to a PEG-P(CL-DTC) polymer solution (300 mg/mL) in DMSO/PEG350 (2/8, v/v) at different drug loading contents (Nap loading content: 1.4 *wt.*%, ICG loading content: 3.4 *wt.*%, 4.6 *wt.*%, 6.8 *wt.*%, and 9.0 *wt.*%). Typically, 100 μL of the pre-mixed solution containing PEG-P(CL-DTC) (14.1 mg) and prescribed ICG and Nap was dropwise added to 900 μL phosphate buffer (PB, pH 7.4, 10 mM) at 37 ℃ followed by gentle mixing, yielding mICG-Nap with different drug loadings. Acupa-functionalized ICG and

Nap-coloaded micelles (Acupa-mICG-Nap) were obtained at ICG/Nap = 1:1 using the same procedure but replacing the polymer with a mixture of 95% PEG-P(CL-DTC) and 5% Acupa-PEG-P(CL-DTC). Micelles containing only ICG (mICG) or no drugs (empty micelles, Ms) were obtained similarly, and a mixture of free ICG and Nap (ICG-Nap) were used as controls.

Size, size distribution and zeta potential of micellar nanodrugs were measured using DLS. Drug loading content (DLC) and drug loading efficiency (DLE) were determined using UV–vis spectrophotometer for ICG and HPLC for Nap. The stability of nanodrugs during storage at -80 ℃ and in the presence of 10% serum was evaluated by tracking size changes. *In vitro* drug release from nanodrugs was studied using dialysis method (MWCO 7000 Da) at 37 ℃. mICG-Nap (polymer conc.: 1 mg/mL, 0.5 mL) was dialyzed against 8 mL release medium (10 mM PB containing 10% FBS, 1% PEG350, 0.1% Tween 80) under three conditions: pH 5.0, pH 7.4, and pH 7.4 with 10 mM glutathione (GSH). At preset intervals (0, 2, 4, 8, 12, and 24 h), 8 mL release medium was taken to quantify ICG and Nap, and 8 mL corresponding fresh buffer was replenished (n = 3). Cumulative drug release profiles were plotted against time.

2.2. Photothermal and photodynamic properties of mICG-Nap in vitro

300 μL of mICG-Nap (ICG conc.: 0, 6.25, 12.5, 25, 50 μg/mL), mICG (ICG conc.: 6.25, 25 μg/mL), free ICG-Nap (ICG conc.: 6.25, 25 μg/mL), free ICG (ICG conc.: 6.25, 25 μg/mL), Ms (polymer conc. 0.54 mg/mL), and PBS were in 96-well plate were irradiated with NIR (808 nm, 1 W/cm^2, 5 min). During the irradiation, temperature of the solutions was recorded every minute (n = 3). Temperature increase of mICG-Nap (300 μL, ICG conc.: 20 μg/mL) irradiated with NIR at different intensities (0.33, 0.67, 1.0, and 1.33 W/cm^2) for 5 min was also studied (n = 3). In all formulations containing both drugs, ICG/Nap molar ratio was fixed at 1/1.

RM1-PSMA cells were seeded on 24-well plate (5×10^5/well) overnight and treated with mICG-Nap, mICG, free ICG, free Nap, or a mixture of ICG-Nap (ICG conc.: 10 μg/mL, Nap

conc.: 3.1 μg/mL) for 2 h (PBS as control). Then DCFH-DA (10 μM) was added to the cells, and cells were irradiated with NIR (808 nm, 1 W/cm^2, 5 min). Cells were washed twice immediately, stained with DAPI (0.5 μg/mL, 5 min) and imaged by fluorescence microscope. Intracellular ROS generation was semi-quantitatively analyzed using Image J software (n = 3).

2.3. Impact of mICG-Nap on the stemness of S-RM1-PSMA cells and tumor spheroids

3D tumor spheroid model were established by culturing RM1-PSMA cells under hypoxic environment. On day 7, tumor spheroids were digested into single cell suspension, called stem-like RM1-PSMA cells (S-RM1-PSMA), and after further culturing the re-formed tumor spheroids (called spheroids) were obtained for further studies.

To examine the inhibitory effect on CSC markers, mICG-Nap (Nap conc.: 0.1 and 0.2 μg/mL) was added to the tumor spheroids. After incubation for two days, the tumor spheroids were digested by accutase into single cell suspension. This was followed by staining with 7-AAD to exclude dead cells, and FITC-CD44 and PE-CD133 antibodies for flow cytometry measurements to determine the contents of $CD44^+CD133^+$ CSCs (n = 3).

To study the impact of mICG-Nap on tumor spheroid formation, S-RM1-PSMA cells were cocultured (200/well) with mICG-Nap (Nap conc.: 0.1 and 0.2 μg/mL) in serum-free medium under hypoxic condition. After 48 h, spheroids were observed using light microscope and counted (> 50 μm, n = 4).

To investigate the effect of mICG-Nap on pre-existing tumor spheroids, mICG-Nap (Nap conc.: 0.1 and 1 μg/mL) were incubated with the spheroids (>50 μm) under hypoxic condition for 2 days, followed by microscopic observation and counting of spheroids (> 100 μm, n = 4).

To investigate the effect of mICG-Nap combined with NIR (mICG-Nap+L) on pre-existing tumor spheroids, spheroids (>50 μm) were incubated with mICG-Nap (Nap conc.: 0.2 μg/mL, ICG conc.: 6.46 and 32.3 μg/mL) for 1 h and then irradiated with NIR (808 nm, 1 W/cm^2, 5 min). Cells were further cultured for 5 days under hypoxic condition, followed by microscopic observation and counting of spheroids (> 200 μm, n = 3).

To determine the down-regulation of stemness-associated genes and proteins, tumor spheroids (>50 μm) were incubated with mICG-Nap or mICG for 1 h and then irradiated with NIR. Spheroids were further cultured for 48 h (n = 3). Half of the cells were subject to protein extraction and 20 μg of proteins were electrophoresed (β-Actin as an internal reference) for western blotting (WB) of STAT3, pSTAT3, OCT4, and SOX2. The other half of cells were subject to RNA isolation for quantitative real-time PCR (qRT-PCR) measurements to determine the expression of *Oct4* and *Sox2* mRNA (*Gapdh* as an internal reference).

2.4 Cellular uptake and cytotoxicity of Acupa-functionalized micelles

Cy5-labeled Acupa-mICG-Nap with Acupa densities of 0%, 1.25%, 2.5%, 5% or 10% were prepared, by pre-mixing PEG-P(CL-DTC)-Cy5, Acupa-PEG-P(CL-DTC) and PEG-P(CL-DTC) (10, 50, 300 mg/mL, respectively) at molar ratios of 1/0/99, 1/1.25/97.75, 1/2.5/96.5, 1/5/94 and 1/10/89, respectively. To study cellular uptake, 100 μL Cy5-labeled formulations were added into RM1-PSMA or RM1 cells in 12-well plates (5×10^5/well). After 2 h, cells were digested by Trypsin-EDTA, centrifuged, washed and measured using flow cytometry (n = 3).

To study the endocytic pathway of micelles, RM1-PSMA cells were pretreated with free Acupa (1.5 mg/mL), dynasore (Dyn, 100 μM), wortmannin (Wor, 1 μM), amiloride (Ami, 100 μM), nystatin (Nys, 20 μM), chlorpromazine (CPZ, 30 μM), or genistein (Gen, 100 μM) for 1 h, or stored at 4 ℃ for 1 h. Then Cy5-labeled Acupa-mICG-Nap was added and incubated for 2 h (Cy5 conc.: 3 μg/mL). Cells were washed and analyzed using flow cytometry (n = 3). Relative uptake was calculated based on uptake by cells pretreated with PBS (100%).

mICG-Nap and Acupa-mICG-Nap (10 μL, ICG conc.: 0.32 - 323 μg/mL; Nap conc.: 0.1 - 100 μg/mL) were added into RM1-PSMA or RM1 cells seeded in 96-well plates (3×10^3/well, 90 μL). After 48 h incubation, cells were added with CCK8 and absorbance at 450 nm was measured using a microplate reader to calculate cell viability (n = 3). For combination therapy with NIR, after 1 h incubation with nanoformulations, cells were irradiated with NIR (L: 808

nm, 1 W/cm^2, 5 min). After 1 h culturing, cell medium was replaced with fresh medium. Following further culture for 46 h, cells were subject to CCK8 assays to calculate cell viability (n = 3).

2.5 Pharmacokinetics studies

All animal procedures were performed in accordance with the Guidelines for Care and Use of Laboratory Animals of Soochow University (P.R. China) and approved by the Animal Ethics Committee of Soochow University (approval no. 202210A0249, 202303A0057, 202405A0545). Healthy male Balb/c nude mice (20 g, 6-week-old) were intravenously injected with Acupa-mICG-Nap, mICG-Nap or free ICG-Nap via tail veins (ICG: 6.46 mg/kg, Nap: 2 mg/kg, n = 3). At predetermined time points (1, 5, 10, 20, 30, 60, 120, 240, and 480 min post-injection), blood was withdrawn from eye socket and centrifuged. 20 μL plasma was mixed with 980 μL acetonitrile (ACN) and vortexed to extract ICG and Nap. Fluorescent intensity of samples was measured using *in vivo* imaging system (IVIS) for determination of ICG. Then samples were centrifuged and supernatants were concentrated using rotary evaporator to 200 μL for Nap quantification using HPLC. Standard curves of ICG and Nap were constructed by using solutions of ICG and Nap with known concentrations in ACN, which were treated with serum using the same procedure as above. Concentrations of drugs were plotted against time and parameters ($t_{1/2,\beta}$ and AUC) were derived by PK Solver.

2.6 Therapeutic efficacy of combination therapies in RM1-PSMA tumor-bearing mice

RM1-PSMA tumor-bearing models were established by inoculating 5×10^5 RM1-PSMA cells (50 μL PBS) into the right flanks of male BALB/c nude mice, and the inoculation day was designated as day 0. On day 7, tumor volume grew into 150-200 mm^3, mice were randomly divided into five groups (n = 5): Acupa-mICG-Nap+L, mICG-Nap+L, mICG+L, mICG-Nap and PBS. On days 7, 9 and 11, Acupa-mICG-Nap, mICG-Nap or mICG (ICG: 6.46 mg/kg, Nap: 2 mg/kg) was *i.v.* injected via tail veins. For combination groups, one hour after each injection, NIR (808 nm, 1 W/cm^2, 5 min) was irradiated on the tumors. Mice

received three *i.v.* PBS injections were used as control. Temperature of tumors was recorded during the first irradiation. Tumor volume and body weight of the mice were monitored every 2 days. Survival rates of the mice were determined when mice died or tumor volume reached 2000 mm^3. One mouse of each group was euthanized and main organs (lung, heart, liver, spleen, and kidney) were stained with hematoxylin and eosin (H&E) for histological evaluation.

2.7 Therapeutic activity of Acupa-mICG-Nap+L in postoperative RM1-PSMA models

Postoperative models were established by surgically removing tumor blocks from the previously built RM1-PSMA tumor-bearing mice on day 7, allowing tumors recurrence or metastasis. On days 9, 11 and 13, mice were *i.v.* injected with Acupa-mICG-Nap (ICG: 6.46 mg/kg, Nap: 2 mg/kg, n = 6), and one hour after each injection, relapsed tumor site was irradiated with NIR (808 nm, 1 W/cm^2, 5 min). Mice after surgery received three *i.v.* PBS injections were used as control. Temperature of tumor sites, tumor volume, body weight, and survival rates of the mice were determined as above. On day 17, one mouse of each group was euthanized and the lung was evaluated using H&E-staining.

To study the impact of Acupa-mICG-Nap+L therapy on the expression of stemness-related biomarkers on tumor cells *in vivo*, immunofluorescence staining studies were performed in the postoperative models using the same dosing scheme and taking Acupa-mICG-Nap and Acupa-mICG monotherapies as control groups. On day 15, tumor slices were prepared and stained separately with SOX2, CD133, OCT4, pSTAT3 and PSMA primary antibodies, followed by treating with Alexa Fluor 488 or Alexa Fluor 647 secondary antibodies and microscopic observation.

2.8 Statistical Analysis

All data were presented as mean ± standard deviation. Statistical differences among groups were assessed by one-way ANOVA with Tukey's multiple comparison tests. Survival

analysis was performed by log-rank (Mantel-Cox) test. The *p* values are depicted as follows: * $p < 0.05$, ** $p < 0.01$, *** $p < 0.001$, **** $p < 0.0001$.

3. Results and Discussion

3.1. Preparation of mICG-Nap and Acupa-mICG-Nap

mICG-Nap could be readily acquired via self-assembly of PEG-P(CL-DTC) copolymer in the presence of ICG and Nap, and PSMA-targeting formulation Acupa-mICG-Nap by further addition of 5% Acupa-PEG-P(CL-DTC) (Scheme 1A). The synthesis of Acupa-functionalized polymer, Acupa-PEG-P(CL-DTC), yielded an Acupa functionality exceeding 85% (Figure S1). Interestingly, micelles at various ICG/Nap molar ratios could be obtained, but only ICG/Nap ≥ 1/1 could yield stable nanoformulations with high drug loading (Table S1). For instance, at an ICG/Nap = 1/1, mICG-Nap could be facilely obtained with over 91% (ICG) and 81% (Nap) drug loading efficiency, and they exhibited a spherical morphology, small hydrodynamic size (ca. 23 nm), and slightly negative zeta potential (Table S1, Figure 1A). Considering the drug loading content and stability, micelles loaded with ICG/Nap at 1/1 molar ratio was chosen for subsequent studies if not stated otherwise. Thus-obtained mICG-Nap, after three months of storage at -80 ℃, exhibited good stability with little change in size and inhibitory effect on tumor cells (Figure S2A,B). Acupa-mICG-Nap had identical physicochemical properties as mICG-Nap (Table S1). Notably, small size of the micellar nanodrugs (23 nm) particularly enabled effective penetration through dense tumor tissues [36, 37], which sequester CSCs. Both mICG-Nap and Acupa-mICG-Nap kept unchanged size and size distributions in 10% serum-containing buffer over 24 h, warranting intravenous injection (Figure 1A, Table S2). The high stability of mICG-Nap might be ascribed to a strong intermolecular interaction between Nap and ICG as well as the disulfide-crosslinked micellar core serving as a physical barrier. The molecular docking simulation study using AutoDock

Vina programme revealed a stable "taco-like" configuration with one Nap molecule embedded within one bending ICG molecule, likely facilitated by π-π stacking, hydrogen bonding, and hydrophobic interactions (Figure 1B). This arrangement effectively inhibits the crystallization and precipitation of Nap from the micelles, excellently addressing the formulation challenge of Nap.

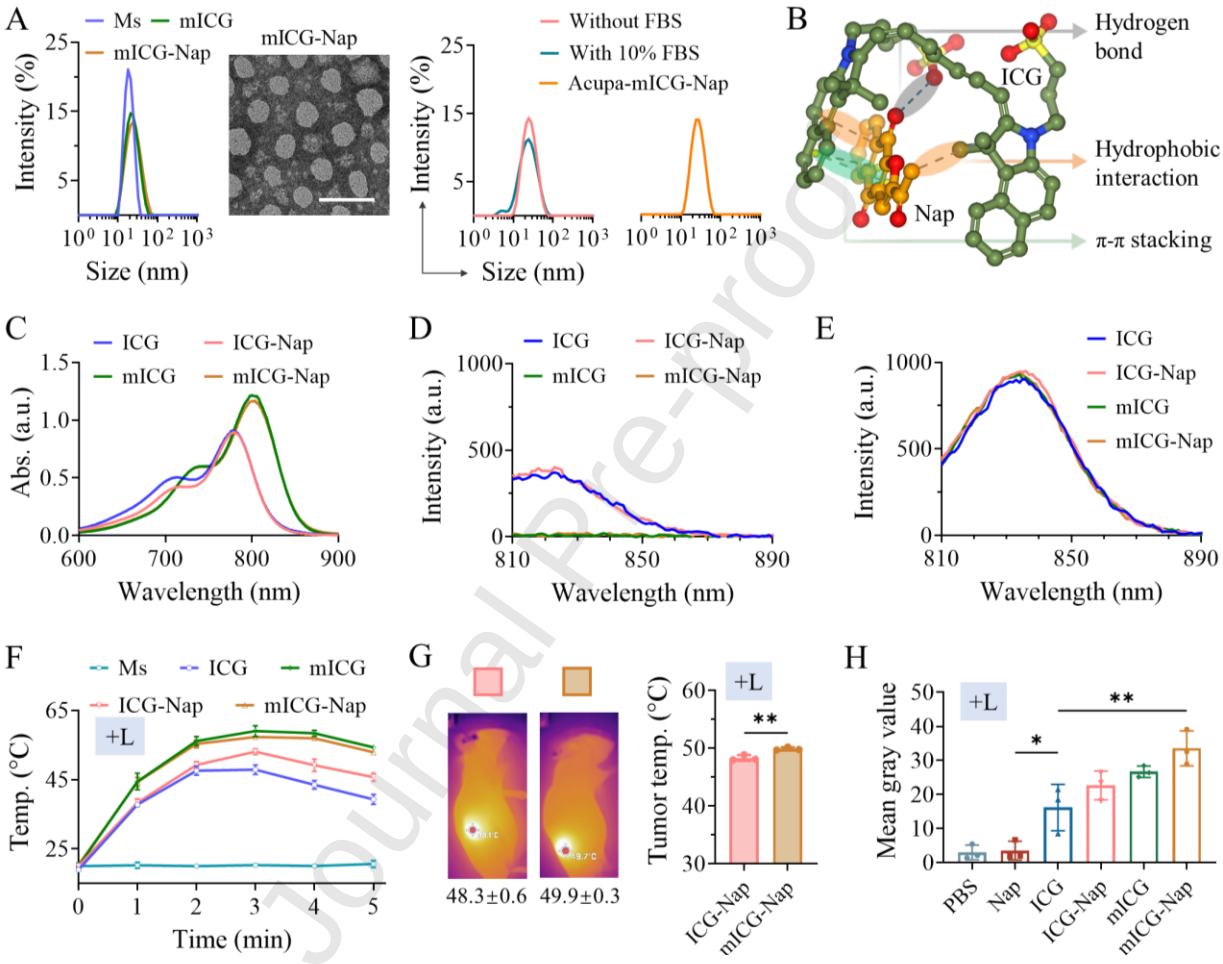

Figure 1. Characterizations of mICG-Nap. (A) Size distribution profiles of freshly prepared mICG-Nap (Inset: TEM micrograph, scale bar: 100 nm) and Acupa-mICG-Nap, and stability after 24 h incubation with PB containing 10% FBS (polymer conc.: 1 mg/mL). (B) Simulation of interaction between ICG and Nap (molar ratio: 1:1) using AutoDock Vina program. (C) UV-vis spectra of mICG-Nap (ICG conc.: 10 μg/mL). Fluorescence spectra of mICG-Nap in (D) phosphate buffer and (E) DMF (Ex: 780 nm, ICG conc.: 20 μg/mL). (F) Temperature elevation of formulations irradiated with NIR (300 μL, ICG conc.: 25 μg/mL, n = 3). (G) Representative thermal images and average temperature of RM-1-PSMA tumors in nude mice at 1 h post intravenous injection mICG-Nap (6.46 mg ICG/kg) (n = 3). (H) Semi-quantitative ROS production in RM-1-PSMA cells treated with mICG-Nap (ICG conc.: 10 μg/mL) using DCF as a label as analysed by Image J (n = 3). mICG, free ICG-Nap and free ICG

were used as control groups. For F, G and H, NIR irradiation (L): 808 nm, 1 W/cm^2, 5 min. * $p < 0.05$, ** $p < 0.01$.

Spectroscopic analyses revealed that both mICG-Nap and mICG exhibited a pronounced red shift in the maximal absorbance peak (from 779 to 803 nm) compared to free ICG and free ICG-Nap mixture (Figure 1C, Figure S2C). The fluorescence of ICG was nearly completely quenched in micelles mICG-Nap and mICG (Figure 1D), which could be recovered when adding DMF (Figure 1E). Under NIR irradiation (Laser: 808 nm, 1 W/cm^2, 5 min), mICG-Nap and mICG exhibited significantly stronger and more durable photothermal effects compared to free ICG (Figure 1F,S2D). The photothermal effect of mICG-Nap depended on ICG concentration and irradiation power (Figure S2E,F). In RM1-PSMA prostate tumor models, intravenous (*i.v.*) injection of mICG-Nap led to more pronounced increase in tumor temperature than free ICG-Nap (**, Figure 1G), signifying enhanced accumulation and retention of mICG-Nap in the tumor. mICG-Nap also induced much more reactive oxygen species (ROS) in cells (Figure 1H), likely originating from a better cellular uptake. Additionally, *in vitro* drug release studies demonstrated that both Nap and ICG were released significantly faster under cytosol mimicking condition (pH 7.4, 10 mM GSH) than under endosome (pH 5.0) and circulation (pH 7.4) mimicking conditions (Figure S2G), attributing to the de-crosslinking of disulfide-crosslinked micelle cores. Triggered release within cytosol is crucial for the inhibition of STAT3 signaling pathway and thus CSC elimination, as well as ROS production.

3.2. mICG-Nap with or without NIR irradiation effectively inhibited CSCs

To investigate the efficacy of mICG-Nap in targeting CSCs, we established a 3D-structured tumor spheroid model to enrich CSC population in RM1-PSMA cells. Specifically, a serum-free culture under anoxic condition was employed and 10,000 cells/mL was inoculated (Figure S3A). By day 7, tumor spheroids reached a maximum diameter of about

570 μm with a notable enrichment of 5.30% $CD44^{+}CD133^{+}$ CSCs, significantly exceeding the 0.84% observed in 2D RM1-PSMA cells (Figure S3B,C), confirming the procedure to obtain CSCs. The cells digested from the tumor spheroids, denoted as S-RM1-PSMA, demonstrated a viability of 97.5% and a CSC proportion of 4.62%, as determined by flow cytometry (FC) (Figure 2A-C). WB results corroborated with highly elevated expression of pSTAT3 and stemness marker OCT4 in S-RM1-PSMA cells compared to RM1-PSMA cells (Figure S3D).

The treatment with mICG-Nap at Nap concentration of 0.2 μg/mL reduced S-RM1-PSMA's viability and CSC proportion (1.74%) (Figure 2B,C) using a gating strategy shown in Figure S4. Remarkably, the CSC suppression capability of mICG-Nap was also demonstrated by significantly inhibiting the formation of colonies and tumor spheroids (****), and destroying pre-existing tumor spheroids (****, Figure 2D,E, Figure S5A), owing to the important role of CSCs in clone formation and proliferation [38].

The anti-CSC activity of mICG-Nap in combination with NIR irradiation (mICG-Nap+L) was then investigated on pre-existing tumor spheroids. The results showed that mICG-Nap+L reduced the number, size and structural integrity of these spheroids, significantly outperforming mICG+L at two ICG concentrations (6.46 and 32.3 μg/mL) and fixed Nap concentration (0.2 μg/mL) (****, Figure 2F). Specifically, at an ICG concentration of 32.3 μg/mL, mICG-Nap+L treatment increased the temperature to 57.7 ℃ and the PTT effect resulted in a strong synergistic effect in eliminating tumor spheroids from day 3. With prolonged treatment duration, the morphology of solid spheroids was progressively altered, becoming irregular and spongy, which likely facilitates deeper penetration of mICG-Nap into the spheroids, promoting the collapse of tumor structure and eradication of CSCs. These results showcased the great effect of mICG-Nap on reducing the stemness of tumor spheroids. Subsequent qRT-PCT and WB measurements confirmed that mICG-Nap+L therapy could remarkably inhibit the mRNA and protein expression levels of OCT4 and SOX2, which were highly upregulated by PTT alone (mICG+L) in S-RM1-PSMA cells (Figure 2G-I). Notably,

mICG-Nap and mICG-Nap+L groups, showing significant reduction in OCT4 and pSTAT3 levels (Figure 2I), substantiate that micellar Nap reduced the stemness by inhibiting the self-renewal and pluripotency of CSCs and by down-regulating STAT3 signaling pathway.

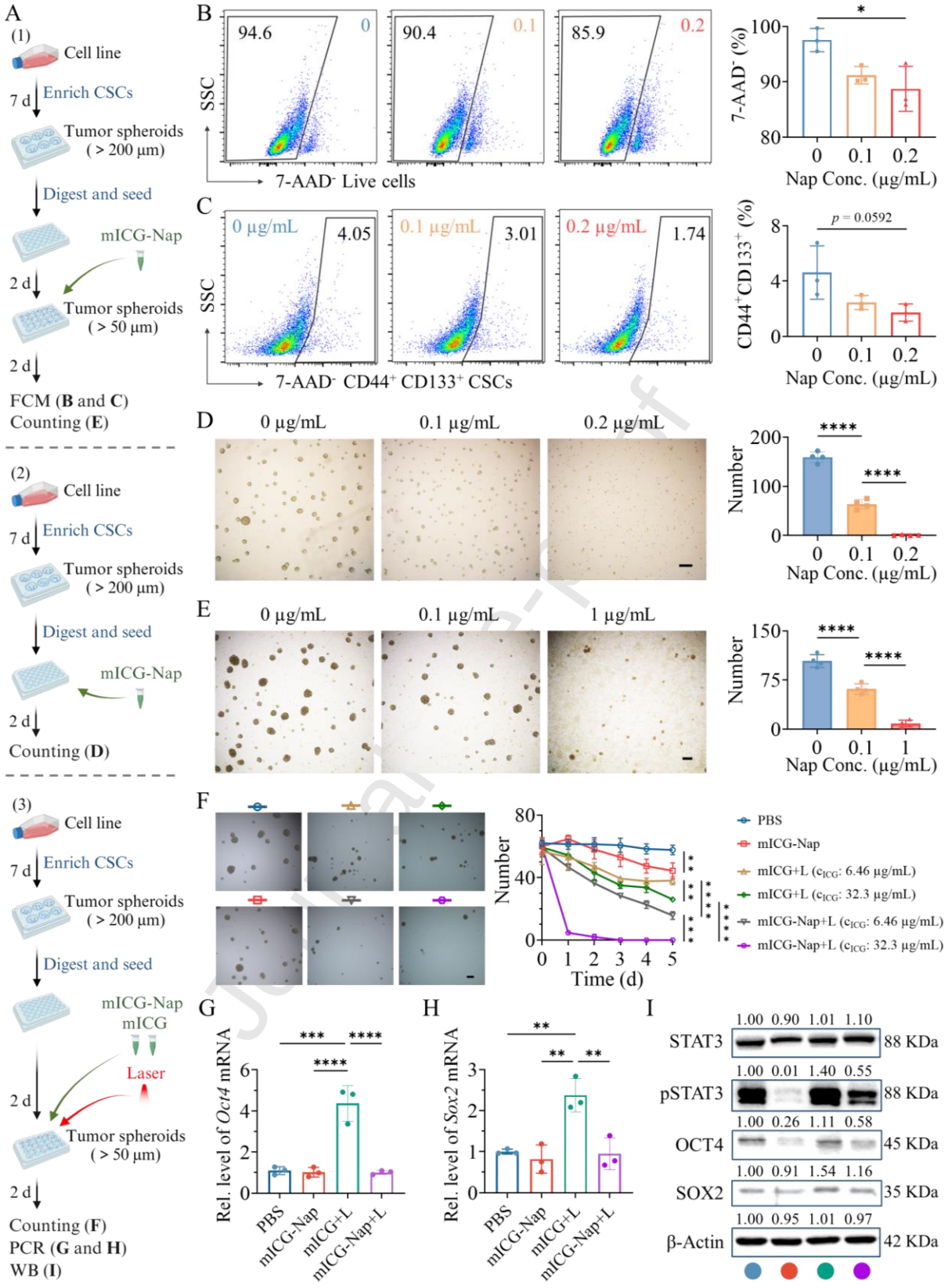

Figure 2. Effects of mICG-Nap on the stemness of S-RM1-PSMA cells. (A) Experimental schemes. Flow cytometric analysis on (B) live cell population (7-AAD$^-$) and (C) CD44$^+$CD133$^+$ cell population of S-RM1-PSMA cells at 48 h incubation with mICG-Nap (n = 3). (D) Images and numbers of tumor spheroids (> 50 μm) formed from a single-cell suspension after 2 days incubation with mICG-Nap

(scale bar: 200 μm, n = 4). (E) Images and numbers of the remaining tumor spheroids (> 100 μm) after 2 days treatment of pre-existing tumor spheroids with mICG-Nap (scale bar: 200 μm, n = 4). (F) Images and numbers of the remaining tumor spheroids (>200 μm) by treatment with mICG-Nap for 1 h, NIR irradiation and subsequent incubation for 5 days under hypoxic environment. mICG+L at various concentrations and mICG-Nap were used as controls (scale bar: 200 μm, n = 3). Expression of (G) *Oct4* mRNA and (H) *Sox2* mRNA (*Gapdh* as internal reference) and (I) expression of STAT3, pSTAT3, OCT4 and SOX2 (β-Actin as internal reference) in S-RM1-PSMA cells treated with mICG-Nap, mICG+L, or mICG-Nap+L. * $p < 0.05$, ** $p < 0.01$, *** $p < 0.001$, **** $p < 0.0001$.

For S-RM1-PSMA cells, CCK8 assay results displayed that mICG-Nap+L showed an obvious reduced half maximal inhibitory concentration (IC_{50}) compared to mICG-Nap and mICG+L alone, illustrating a moderate synergistic effect (combination index of 0.8) (Figure S5B). This enhanced activity can be attributed to ROS production of the formulations (Figure 1H), as no obvious photothermal effect was observed (temperature increase < 7 ℃) at ICG ≤ 3.23 μg/mL. Apoptosis assays were conducted on S-RM1-PSMA cells using mICG-Nap+L with various concentrations of Nap and ICG (Figure S5C). At ICG = 2.6 μg/mL, mICG-Nap+L group showed higher total apoptosis levels compared to either mICG-Nap or mICG+L group. While at ICG = 13 μg/mL, mICG-Nap+L induced a temperature increase into 44.9 ℃ (PTT effect occurred), leading to an over two-fold greater apoptosis. Notably, Nap exhibited substantially more impact on late apoptosis compared to thermal effect on S-RM1-PSMA cells.

3.3. mICG-Nap+L therapy halted progression of prostate tumor models

Inspired by the promising results of CSC suppression, we investigated the therapeutic activity of mICG-Nap+L treatment in subcutaneous RM1-PSMA tumor-bearing mice, via intratumoral (*i.t.*) or intravenous (*i.v.*) injection route (Figure S6A). The PBS group exhibited rapid tumor growth, reaching 2000 mm^3 (designated dead) within ca. 13 d. In the *i.t.* group, tumors initially disappeared by day 9 but rapidly relapsed by day 13 (Figure S6B,C). Despite receiving a second *i.t.* injection on day 19, tumor growth could not be effectively halted,

yielding a median survival time (MST) of 31.5 days (**, Figure S6D). Additionally, lung metastasis was observed in this group (Figure S6E), consistent with reports showing PTT-induced tumor metastasis, particularly following *i.t.* administration [39]. In striking contrast, the *i.v.* group maintained small tumor volumes for an extended period, achieving a MST of 67 days without noticeable metastasis. This favorable outcome may be attributed to the effects of Nap delivered intravenously by ICG and micelles, which targeted and eliminated the local CSCs within tumor and escaped CSCs.

Based on the above proof-of-concept study, we conducted a systematic investigation of the antitumor activity of mICG-Nap+L using *i.v.* injection (Figure 3A). Tumor growth curves showed that only eliminating CSCs using three *i.v.* injections of mICG-Nap could hardly suppress the rapidly growing tumors (Figure. 3B). Only PTT with mICG+L resulted in great tumor inhibition during the first 3 weeks without body weight changes, however, tumors subsequently recurred (Figure. 3B,C), as commonly observed in PTT ablation therapies [25]. In striking contrast, the combination therapy mICG-Nap+L demonstrated significantly enhanced tumor suppression, with an 80% tumor-elimination with 45 days. The MST was significantly prolonged to 55 days compared to 43 days for mICG+L group (*, Figure. 3D), despite of similar tumor temperature (Figure. 3E). Additionally, histological analysis revealed that mICG-Nap+L treatment did not damage lung structure, unlike the thickened alveolar wall of mICG+L group (Figure. 3F). The efficacy of Nap in suppressing tumor growth was previously documented, exhibiting tumor suppression in mice at doses of 40 mg/kg (*i.p.*) administered every other day for glioblastoma or 20 mg/kg (*i.p.*) every three days for pancreatic cancer [40, 41]. Remarkably, mICG-Nap+L strategy demonstrate outstanding antitumor efficacy at 2 mg Nap/kg (total 3 doses), underscoring the strong synergistic effects of PTT-mediated tumor ablation and the selective elimination of CSCs *in vivo*.

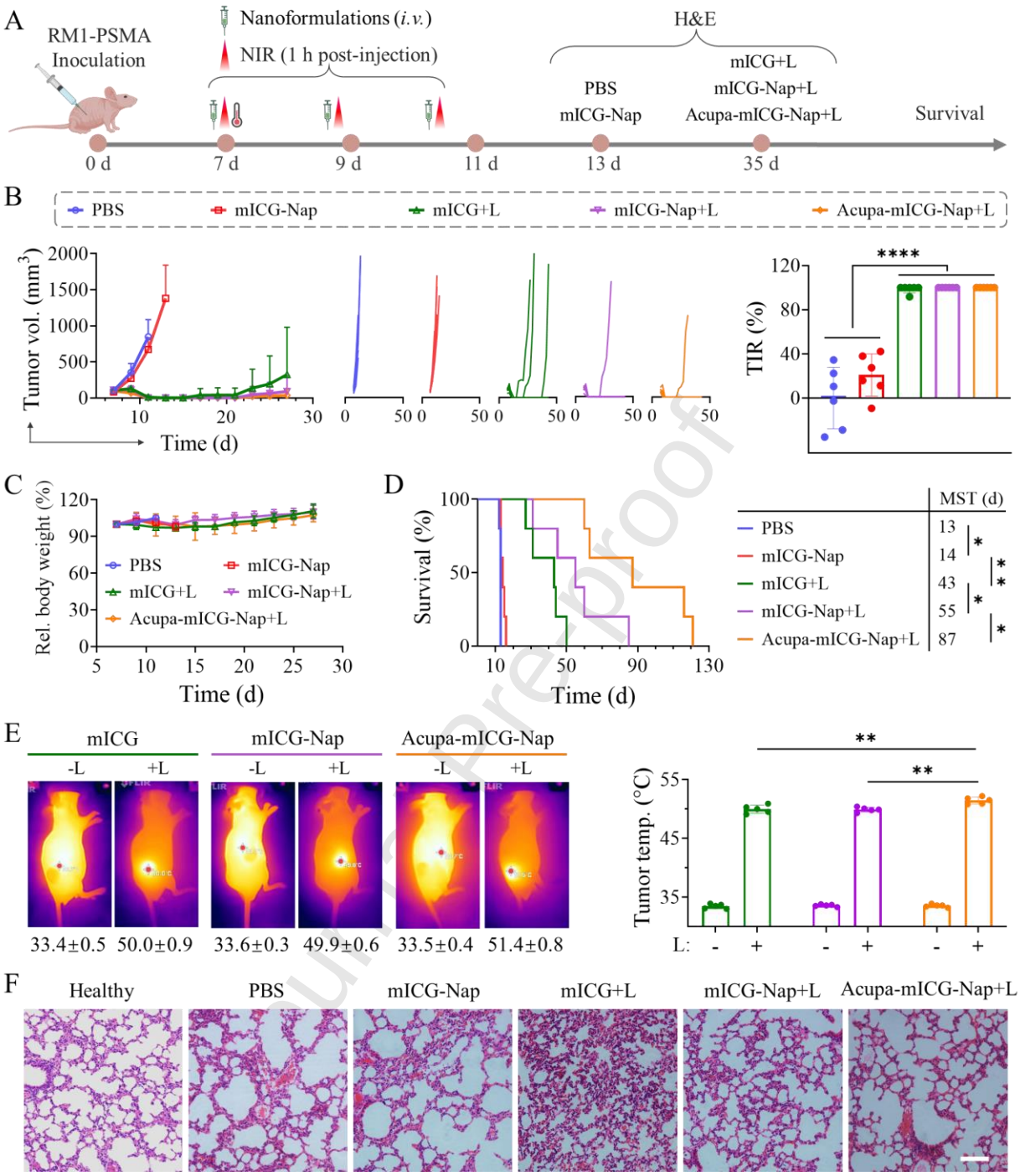

Figure 3. Therapeutic activity of combination therapies of mICG-Nap+L and Acupa-mICG-Nap+L in RM1-PSMA tumor-bearing mice. (A) Experimental schedule. ICG dose: 6.46 mg/kg, Nap dose: 2 mg/kg (ICG/Nap molar ratio of 1/1); NIR (L: 808 nm, 1 W/cm^2, 5 min). (B) Tumor growth curves and tumor inhibition rate (TIR) on day 11. (C) Relative body weight and (D) survival rates of the mice (n = 5). PBS, mICG-Nap and mICG+L were used as controls. (E) Infrared thermal images of the mice and tumor temperature upon the first irradiation (n = 5). (F) H&E-stained images of lung slices (scale bar: 100 μm). * $p < 0.05$, ** $p < 0.01$, **** $p < 0.0001$.

3.4. Acupa-mICG-Nap+L significantly extended the survival of RM1-PSMA mice

To further enhance the performance, we investigated the *in vivo* antitumor efficacy of PSMA-targeting Acupa-mICG-Nap. PSMA overexpresses in prostate cancer cells and is a well-validated target, and Acupa has been established in clinical trials as an effective PSMA-targeting ligand [34]. FC assays confirmed that RM1-PSMA cells, genetically engineered RM-1 cells with human PSMA [42], demonstrated significantly higher PSMA expression than RM-1, PC-3 and LNCaP cells (Figure 4A). The cellular uptake of Cy5-labeled Acupa-mICG-Nap containing 5% Acupa by RM1-PSMA cells was the highest, and ca. 2.2-fold increase compared to mICG-Nap (Figure 4B). Conversely, in PSMA low-expressing RM1 cells, both mICG-Nap and Acupa-mICG-Nap showed similar uptake (Figure 4B), underscoring the targeting effect of Acupa. Studies on endocytic pathway of Acupa-mICG-Nap indicated that macropinocytosis and caveolae played important roles in mediating its endocytosis in addition to PSMA-Acupa (receptor-ligand) interactions (Figure 4C). Based on these results, Acupa-mICG-Nap with 5% Acupa was used for subsequent studies.

MTT assays further showed that Acupa-mICG-Nap and Acupa-mICG-Nap+L caused much more death of RM1-PSMA cells than their corresponding non-targeting counterparts, but no difference in RM-1 cells, with empty micelles being nontoxic (Figure 4E-G). Notably, the pharmacokinetic analysis displayed a greatly prolonged circulation for both ICG and Nap when delivered by Acupa-mICG-Nap and mICG-Nap, with half elimination time ($t_{1/2}$) increased by 8.3- to 54-fold (Figure 4H). Moreover, Acupa-mICG-Nap demonstrated enhanced deposition within tumors of RM1-PSMA-bearing models compared to mICG-Nap at 3, 6 and 24 h post-injection, while there was no significant difference in main organs for two groups (Figure S7). Despite the ICG signals in the kidneys observed at 24 h, potentially due to premature drug release into circulation, no significant renotoxicity was evident from H&E staining (Figure S8). Remarkably, in RM1-PSMA tumor-bearing mice, the Acupa-mICG-Nap+L treatment resulted in a tumor temperature of 51.4 ℃ (Figure 3E), which is 1.5 ℃

higher compared to mICG+L and mICG-Nap+L treatments (**), likely due to higher tumor accumulation and retention. Such treatment achieved a significantly extended MST (87 days) compared to mICG-Nap+L (55 days) and mICG+L (43 days) groups (*, Figure 3D). Additionally, this group had healthy lung structure without lung metastasis (Figure 3F). H&E staining images of main organs revealed no obvious damages post repeated doses (Figure S8). These results collectively validate the *in vivo* active targetability of Acupa-mICG-Nap and the therapeutic effect of Acupa-mICG-Nap+L on survival benefit.

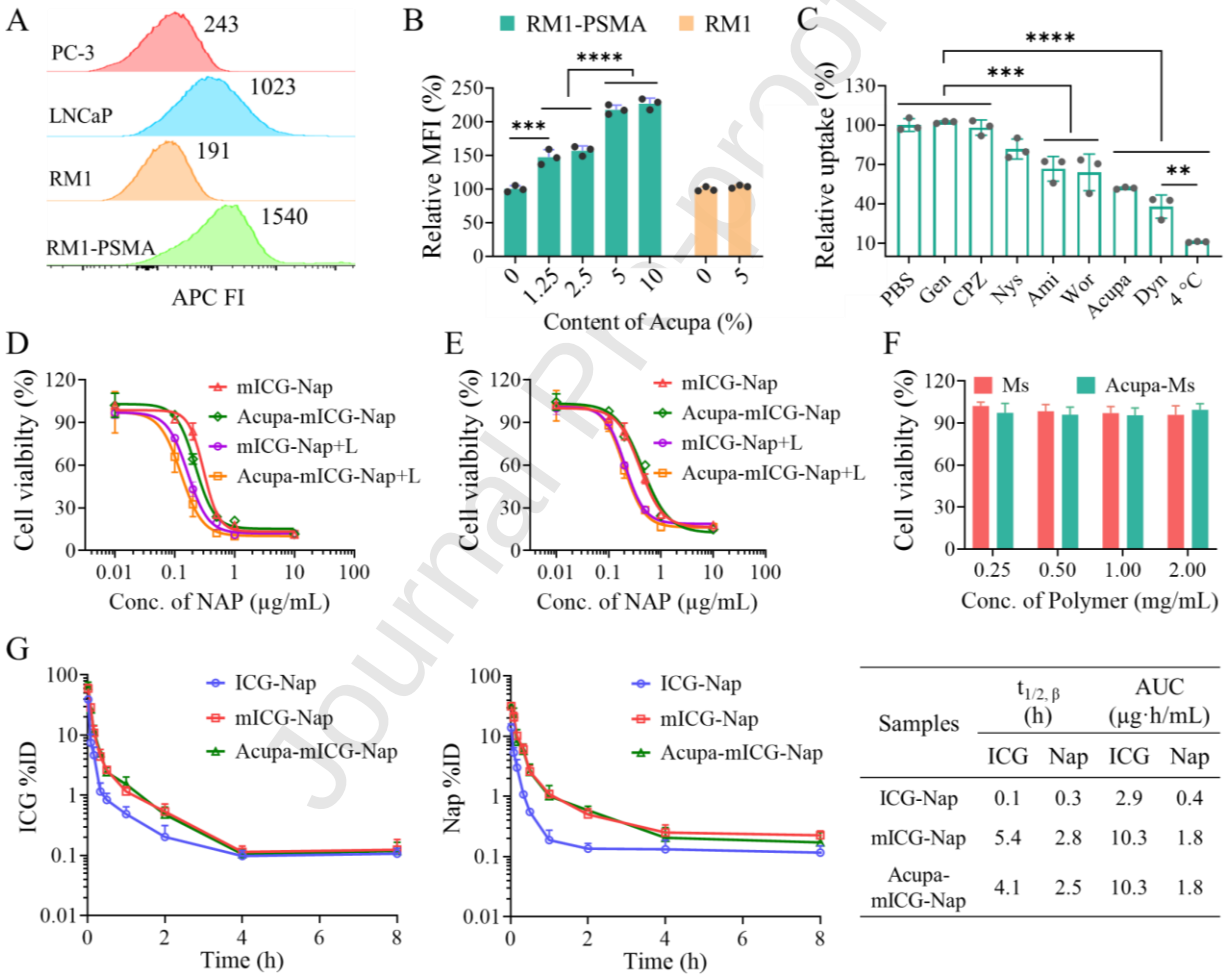

Samples	$t_{1/2,\beta}$ (h)		AUC (μg·h/mL)	
	ICG	Nap	ICG	Nap
ICG-Nap	0.1	0.3	2.9	0.4
mICG-Nap	5.4	2.8	10.3	1.8
Acupa-mICG-Nap	4.1	2.5	10.3	1.8

Figure 4. Cell experiments and pharmacokinetic studies of Acupa-mICG-Nap. (A) Flow cytometry determination of PSMA expression in various cells. (B) Cellular uptake of Cy5-labeled Acupa-mICG-Nap with 1.25%, 2.5%, 5%, or 10% Acupa in RM1-PSMA cells, and with 5% Acupa in RM1 cells (n = 3). (C) Analysis of endocytic pathway of Acupa-mICG-Nap (n = 3). Cytotoxicity of Acupa-mICG-Nap+L and Acupa-mICG-Nap in (D) RM1-PSMA cells and (E) RM1 cells (n = 3). (F) Viability of RM1-PSMA cells treated with empty micelles (n = 6). (G) Pharmacokinetics of Acupa-mICG-Nap, mICG-Nap and free ICG-Nap in RM-1-PSMA tumor-bearing mice after a single *i.v.* injection (ICG:

6.46 mg/kg, Nap: 2 mg/kg, n = 3), using IVIS and HPLC for determination of ICG and Nap, respectively, and parameters ($t_{1/2, \beta}$ and AUC) calculated by PK Solver. ** $p < 0.01$, *** $p < 0.001$, **** $p < 0.0001$.

A first-line clinical drug for prostate cancer, docetaxel (DTX), was utilized to prepare micellar nanodrugs, Acupa-mDTX and mDTX. Acupa-mDTX had similar size (22 nm) and exhibited enhanced cytotoxicity and apoptosis compared to mDTX (Figure S9A-C), and only prolonged MST to 26 days in same RM1-PSMA models (Figure S9D-F). These results underscore the superior performance of Acupa-mICG-Nap+L therapy.

3.5. Acupa-mICG-Nap+L strategy inhibited relapse in postoperative tumor models

Relapse and metastasis to lungs or bones frequently occur in prostate cancer patients following surgery [43, 44]. To evaluate the efficacy of Acupa-mICG-Nap+L therapy in a postoperative context, we established a postoperative RM1-PSMA models by excising tumors on day 7 and treatment started two days later (Figure 5A). The PBS group showed rapid tumor reoccurrence and reached 1300 mm^3 in 6 days post-surgery with constant body weight (Figure 5B,C), leading to a slightly longer MST of 15 days compared to mice without surgery (13 days, Figure 5D). Lung metastasis was observed in H&E images in this group (Figure 5E), indicative of surgery-driven metastasis [43]. Remarkably, Acupa-mICG-Nap+L therapy increased the temperature of relapsed tumors to 51.8 ℃, signifying the accumulation of micellar nanodrugs within relapsed tumors. This treatment significantly restrained tumor growth (****) without observable lung metastasis by day 17 (Figure 5B-F), achieving considerably extended MST to 24 days (***) in this refractory model. The much shorter lifespan of this postoperative model lies in the rapid tumor relapse and metastasis. It is reported that surgical intervention may prompt residual tumor cells to transform into CSC-like states, leading to elevated CSC contents than in primary tumor, contributing to relapse and distal metastasis [44, 45] and a quicker tumor progression.

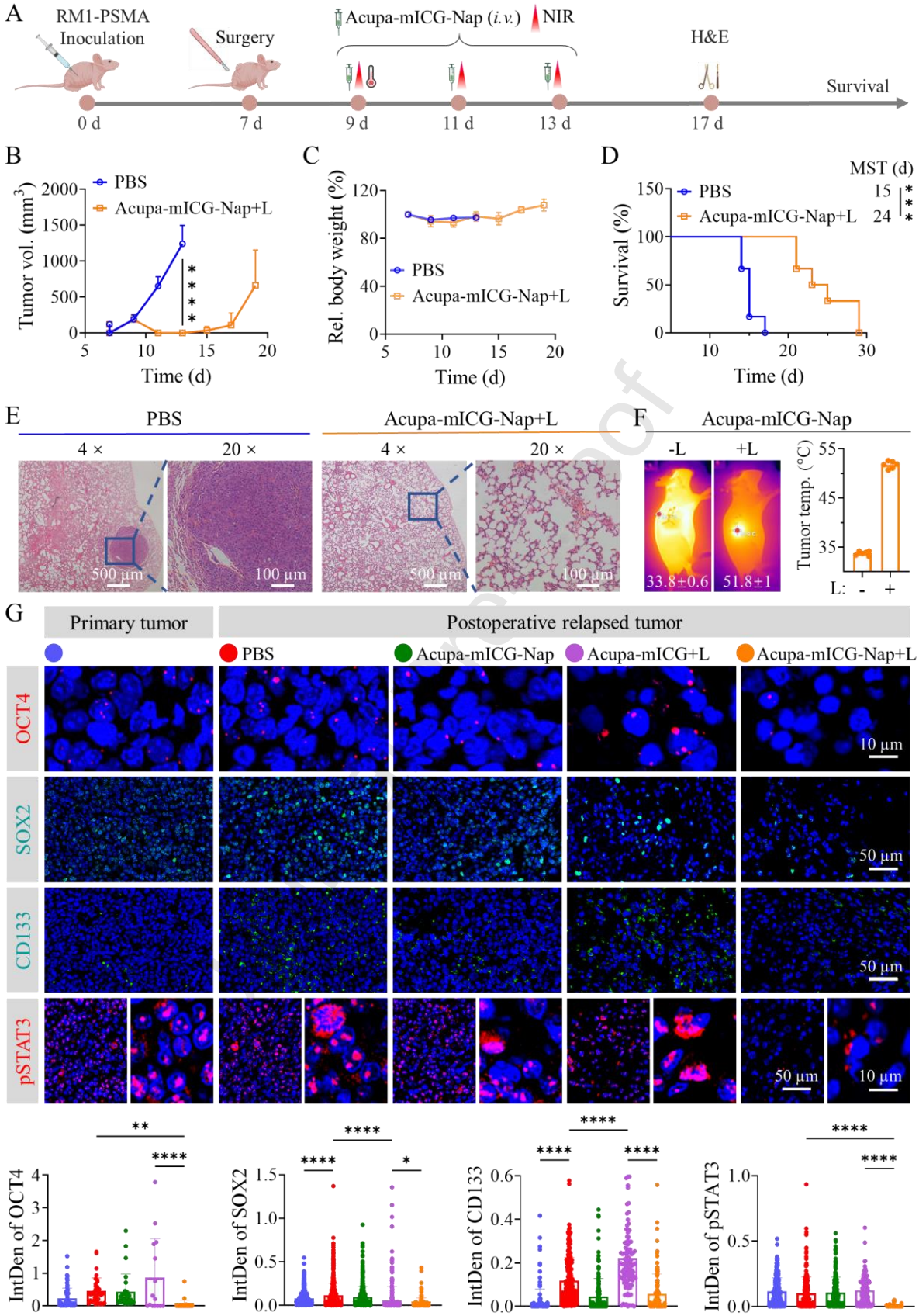

Figure 5. Anti-tumor efficacy of Acupa-mICG-Nap+L strategy in postoperative RM1-PSMA model. (A) Experimental schedule. ICG dose: 6.46 mg/kg, Nap dose: 2 mg/kg (ICG/Nap molar ratio of 1/1); NIR (1 h post-injection, L: 808 nm, 1 W/cm^2, 5 min). (B) growth curves of relapsed tumors, (C)

relative body weight and (D) survival rates of the mice (n = 6). (E) H&E-staining images of lung slices on day 17. (F) *In vivo* thermal images of the mice and temperature of relapsed tumor on day 9 (n = 6). (G) HIF images and semi-quantitative analysis of fluorescence intensity of the expression OCT4, SOX2, CD133 and pSTAT3 in the slices of primary tumors (day 7) and relapsed tumors (day 15) received various treatments. * $p < 0.05$, ** $p < 0.01$, *** $p < 0.001$, **** $p < 0.0001$.

Furthermore, the effect of Acupa-mICG-Nap+L therapy on CSC elimination in this postoperative model was assessed by analyzing the expression of pSTAT3 and stemness-associated proteins, including OCT4, SOX2 and CD133 using histological immunofluorescent (HIF) staining. Previous studies have linked OCT4 to promoting self-renewal and SOX2 to enhanced metastasis potential [46]. The slices of relapsed tumors in PBS group showed significantly higher levels of SOX2 and CD133 compared to primary tumor without surgery (Figure5G). In comparison, Acupa-mICG+L group exhibited considerably increased expressions of OCT4, SOX2 and CD133, confirming the inclined stemness following PTT ablation alone, while these markers were somewhat reduced in Acupa-mICG-Nap group. In sharp contrast, in Acupa-mICG-Nap+L group, three CSC markers were all drastically diminished and tumor cells became much sparser, validating the inhibition capacity of both tumor cells and CSCs.

Interestingly, contrasting to the high levels and localization of pSTAT3 in the nuclei of tumor cells in Acupa-mICG+L and control groups, Acupa-mICG-Nap+L group unveiled overwhelming capability of suppressing pSTAT3 and a decreased colocalization of pSTAT3 with nuclei (****, Figure 5G). This results highlight the highly efficient intracellular delivery of Nap enable by Acupa-mICG-Nap and the effective inhibition of STAT3 signaling pathway, thus preventing transmission of transcriptional signals to the nuclei. It is known that upregulation of STAT3 pathway leads to proliferation, anti-apoptosis, and immunosuppressive microenvironments of many tumor types and is associated with poor

prognosis. Concomitantly, PSMA expression was greatly decreased by Acupa-mICG-Nap+L treatment, likely due to the competitive binding of Acupa to PSMA (Figure S10).

4. Conclusion

We have engineered a robust micellar nanomedicine codelivering ICG and Nap (mICG-Nap) for localized ablation of prostate tumors and targeted eradication of CSCs under NIR irradiation. mICG-Nap significantly reduced CSCs within TME and suppressed CSC-driven tumor spheroid formation. The combination therapy of mICG-Nap+L synergistically reduced the size and number of pre-existing tumor spheroids, outperforming monotherapies. In RM1-PSMA models, mICG-Nap+L resulted in effective inhibition of tumor growth and highlighted a potent synergistic antitumor effect. Notably, the incorporation of PSMA-targeting ligand Acupa into Acupa-mICG-Nap further increased the cellular uptake and cytotoxicity against prostate cancer cells. The small size (23 nm) combined with the binding of Acupa to tumor tissues facilitated superior tumor penetration and retention. Consequently, Acupa-mICG-Nap+L therapy achieved a higher elevation in tumor temperature during PTT, leading to significantly prolonged survival in RM1-PSMA models and also demonstrating great efficacy in postoperative tumor models. Overall, by combining precise local tumor PTT ablation and targeted CSC elimination, Acupa-mICG-Nap+L therapy showcases promising treatment of various solid tumors by addressing the critical challenges of tumor recurrence and metastasis associated with conventional therapies.

Acknowledgements

This work is supported by research grants from the National Natural Science Foundation of China (NSFC 52473142, 52033006).

Conflict of Interest

The authors declare no conflict of interest.

References

[1] R.L. Siegel, A.N. Giaquinto, A. Jemal, Cancer statistics, 2024, CA Cancer J. Clin. 74(1) (2024) 12-49.

[2] S. Sandhu, C.M. Moore, E. Chiong, H. Beltran, R.G. Bristow, S.G. Williams, Prostate cancer, Lancet 398(10305) (2021) 1075-1090.

[3] L. Klotz, C. O'Callaghan, K. Ding, P. Toren, D. Dearnaley, C.S. Higano, E. Horwitz, S. Malone, L. Goldenberg, M. Gospodarowicz, J.M. Crook, Nadir Testosterone Within First Year of Androgen-Deprivation Therapy (ADT) Predicts for Time to Castration-Resistant Progression: A Secondary Analysis of the PR-7 Trial of Intermittent Versus Continuous ADT, J. Clin. Oncol. 33(10) (2015) 1151-1156.

[4] X. Chen, Q. Li, X. Liu, C. Liu, R. Liu, K. Rycaj, D. Zhang, B. Liu, C. Jeter, T. Calhoun-Davis, K. Lin, Y. Lu, H.-P. Chao, J. Shen, D.G. Tang, Defining a Population of Stem-like Human Prostate Cancer Cells That Can Generate and Propagate Castration-Resistant Prostate Cancer, Clin. Cancer Res. 22(17) (2016) 4505-4516.

[5] P. Verma, N. Shukla, S. Kumari, M.S. Ansari, N.K. Gautam, G.K. Patel, Cancer stem cell in prostate cancer progression, metastasis and therapy resistance, Biochim. Biophys. Acta Rev. Cancer 1878(3) (2023) 188887.

[6] P.P. Kushwaha, S. Verma, S. Kumar, S. Gupta, Role of prostate cancer stem-like cells in the development of antiandrogen resistance, Cancer Drug Resist. 5(2) (2022) 459-471.

[7] K. Kise, Y. Kinugasa-Katayama, N. Takakura, Tumor microenvironment for cancer stem cells, Adv. Drug Del. Rev. 99 (2016) 197-205.

[8] L. Yang, P. Shi, G. Zhao, J. Xu, W. Peng, J. Zhang, G. Zhang, X. Wang, Z. Dong, F. Chen, H. Cui, Targeting cancer stem cell pathways for cancer therapy, Signal Transduct. Target Ther. 5(1) (2020) 8.

[9] H.-M. Zhou, J.-G. Zhang, X. Zhang, Q. Li, Targeting cancer stem cells for reversing therapy resistance: mechanism, signaling, and prospective agents, Signal Transduct. Target Ther. 6(1) (2021) 62.

[10] R. Scatena, P. Bottoni, A. Pontoglio, B. Giardina, Cancer stem cells: the development of new cancer therapeutics, Expert Opin. Biol. Ther. 11(7) (2011) 875-892.

[11] W. Tong, L. Qiu, M. Qi, J. Liu, K. Hu, W. Lin, Y. Huang, J. Fu, GANT-61 and GDC-

0449 induce apoptosis of prostate cancer stem cells through a GLI-dependent mechanism, J. Cell. Biochem. 119(4) (2018) 3641-3652.

[12] J. Pencik, C. Philippe, M. Schlederer, E. Atas, M. Pecoraro, S. Grund-Gröschke, W. Li, A. Tracz, I. Heidegger, S. Lagger, K. Trachtová, M. Oberhuber, E. Heitzer, O. Aksoy, H.A. Neubauer, B. Wingelhofer, A. Orlova, N. Witzeneder, T. Dillinger, E. Redl, G. Greiner, D. D'Andrea, J.R. Östman, S. Tangermann, I. Hermanova, G. Schäfer, F. Sternberg, E.E. Pohl, C. Sternberg, A. Varady, J. Horvath, D. Stoiber, T.I. Malcolm, S.D. Turner, E.E. Parkes, B. Hantusch, G. Egger, S. Rose-John, V. Poli, S. Jain, C.W.D. Armstrong, G. Hoermann, V. Goffin, F. Aberger, R. Moriggl, A. Carracedo, C. McKinney, R.D. Kennedy, H. Klocker, M.R. Speicher, D.G. Tang, A.A. Moazzami, D.M. Heery, M. Hacker, L. Kenner, STAT3/LKB1 controls metastatic prostate cancer by regulating mTORC1/CREB pathway, Mol. Cancer 22(1) (2023) 133.

[13] S. Singh, H.J. Gomez, S. Thakkar, S.P. Singh, A.S. Parihar, Overcoming Acquired Drug Resistance to Cancer Therapies through Targeted STAT3 Inhibition, Int. J. Mol. Sci. 24(5) (2023) 4722.

[14] D.J. Jonker, L. Nott, T. Yoshino, S. Gill, J. Shapiro, A. Ohtsu, J. Zalcberg, M.M. Vickers, A.C. Wei, Y. Gao, N.C. Tebbutt, B. Markman, T. Price, T. Esaki, S. Koski, M. Hitron, W. Li, Y.Z. Li, N.M. Magoski, C.J. Li, J. Simes, D.S. Tu, C.J. O'Callaghan, Napabucasin versus placebo in refractory advanced colorectal cancer: a randomised phase 3 trial, Lancet Gastroenterol. Hepatol. 3(4) (2018) 263-270.

[15] Z. Shao, H. Wang, H. Ren, Y. Sun, X. Chen, The Anticancer Effect of Napabucasin (BBI608), a Natural Naphthoquinone, Molecules 28(15) (2023) 5678.

[16] A. Kawazoe, Y. Kuboki, E. Shinozaki, H. Hara, T. Nishina, Y. Komatsu, S. Yuki, M. Wakabayashi, S. Nomura, A. Sato, T. Kuwata, M. Kawazu, H. Mano, Y. Togashi, H. Nishikawa, T. Yoshino, Multicenter Phase I/II Trial of Napabucasin and Pembrolizumab in Patients with Metastatic Colorectal Cancer (EPOC1503/SCOOP Trial), Clin. Cancer Res. 26(22) (2020) 5887-5894.

[17] T. Bekaii-Saab, T. Okusaka, D. Goldstein, D.-Y. Oh, M. Ueno, T. Ioka, W. Fang, E.C. Anderson, M.S. Noel, M. Reni, H.J. Choi, J.S. Goldberg, S.C. Oh, C.-P. Li, J. Tabernero, J. Li, E. Foos, C. Oh, E. Van Cutsem, Napabucasin plus nab-paclitaxel with gemcitabine versus nab-paclitaxel with gemcitabine in previously untreated metastatic pancreatic adenocarcinoma: an adaptive multicentre, randomised, open-label, phase 3, superiority trial, eClinicalMedicine 58 (2023) 101897.

[18] M.A. Shah, T. Yoshino, N.C. Tebbutt, A. Grothey, J. Tabernero, R.-H. Xu, A. Cervantes,

S.C. Oh, K. Yamaguchi, M. Fakih, A. Falcone, C. Wu, V.K. Chiu, J. Tomasek, J. Bendell, M. Fontaine, M. Hitron, B. Xu, J. Taieb, E. Van Cutsem, Napabucasin Plus FOLFIRI in Patients With Previously Treated Metastatic Colorectal Cancer: Results From the Open-Label, Randomized Phase III CanStem303C Study, Clin. Colorectal Cancer 22(1) (2023) 100-110.

[19] M.A. Shah, K. Shitara, F. Lordick, Y.-J. Bang, N.C. Tebbutt, J.-P. Metges, K. Muro, K.-W. Lee, L. Shen, S. Tjulandin, J.L. Hays, N. Starling, R.-H. Xu, K. Sturtz, M. Fontaine, C. Oh, E.M. Brooks, B. Xu, W. Li, C.J. Li, L. Borodyansky, E. Van Cutsem, Randomized, Double-Blind, Placebo-Controlled Phase III Study of Paclitaxel ± Napabucasin in Pretreated Advanced Gastric or Gastroesophageal Junction Adenocarcinoma, Clin. Cancer Res. 28(17) (2022) 3686-3694.

[20] P.K. Vaddi, M.A. Stamnes, H. Cao, S. Chen, Elimination of SOX2/OCT4-Associated Prostate Cancer Stem Cells Blocks Tumor Development and Enhances Therapeutic Response, Cancers (Basel) 11(9) (2019) 1331.

[21] S. Shen, X. Xu, S. Lin, Y. Zhang, H. Liu, C. Zhang, R. Mo, A nanotherapeutic strategy to overcome chemotherapeutic resistance of cancer stem-like cells, Nat. Nanotechnol. 16(1) (2021) 104-113.

[22] Z. Dong, K. Xue, A. Verma, J. Shi, Z. Wei, X. Xia, K. Wang, X. Zhang, Photothermal therapy: a novel potential treatment for prostate cancer, Biomater. Sci. 12(10) (2024) 2480-2503.

[23] X. Li, J.F. Lovell, J. Yoon, X. Chen, Clinical development and potential of photothermal and photodynamic therapies for cancer, Nat. Rev. Clin. Oncol. 17(11) (2020) 657-674.

[24] D.I. Jeong, H.J. Kim, S.Y. Lee, S. Kim, J.W. Huh, J.-H. Ahn, M. Karmakar, H.-J. Kim, K. Lee, J. Lee, H.-J. Ko, H.-J. Cho, Hydrogel design to overcome thermal resistance and ROS detoxification in photothermal and photodynamic therapy of cancer, J. Control. Release 366 (2024) 142-159.

[25] X. Li, T. Yong, Z. Wei, N. Bie, X. Zhang, G. Zhan, J. Li, J. Qin, J. Yu, B. Zhang, L. Gan, X. Yang, Reversing insufficient photothermal therapy-induced tumor relapse and metastasis by regulating cancer-associated fibroblasts, Nat. Commun. 13(1) (2022) 2794.

[26] L. Wang, S. Bi, Z. Li, A. Liao, Y. Li, L. Yang, X. Zhou, Y. Gao, X. Liu, Y. Zou, X. Zhang, J. Shi, S. Yu, Z. Yu, J. Guo, Napabucasin deactivates STAT3 and promotes mitoxantrone-mediated cGAS-STING activation for hepatocellular carcinoma chemo-immunotherapy, Biomaterials 313 (2025) 122766.

[27] B. Jing, F. Guo, R. An, Y. Gao, Y. Li, Y. Xie, J. Wang, Y. Chen, H. Li, T. Gao, Q. Jin, L.

Zhang, M. Xie, Apoptotic tumor cell-derived microparticles loading Napabucasin inhibit CSCs and synergistic immune therapy, J. Nanobiotechnology 21(1) (2023) 37.

[28] T. Gao, S. Yuan, S. Liang, X. Huang, J. Liu, P. Gu, S. Fu, N. Zhang, Y. Liu, In Situ Hydrogel Modulates cDC1-Based Antigen Presentation and Cancer Stemness to Enhance Cancer Vaccine Efficiency, Adv. Sci. 11(20) (2024) e2305832.

[29] B. Guo, Y. Qu, Y. Sun, S. Zhao, J. Yuan, P. Zhang, Z. Zhong, F. Meng, Co-delivery of gemcitabine and paclitaxel plus NanoCpG empowers chemoimmunotherapy of postoperative "cold" triple-negative breast cancer, Bioact. Mater. 25 (2023) 61-72.

[30] D. Ni, B. Guo, Z. Zhong, Y. Chen, G. Yang, J. Yang, Z. Zhong, F. Meng, Integrin-targeting disulfide-crosslinked micellar docetaxel eradicates lung and prostate cancer patient-derived xenografts, Acta Biomater. 170 (2023) 228-239.

[31] X. Qiu, Y. Qu, B. Guo, H. Zheng, F. Meng, Z. Zhong, Micellar paclitaxel boosts ICD and chemo-immunotherapy of metastatic triple negative breast cancer, J. Control. Release 341 (2022) 498-510.

[32] K. Jewell, M.S. Hofman, J.S.L. Ong, S. Levy, Emerging Theranostics for Prostate Cancer and a Model of Prostate-specific Membrane Antigen Therapy, Radiology 311(1) (2024) e249017.

[33] Z. Huangfu, J. Yang, J. Sun, B. Xu, L. Tao, J. Wu, F. Wang, G. Wang, F. Meng, Z. Zhong, PSMA and Sigma-1 receptor dual-targeted peptide mediates superior radionuclide imaging and therapy of prostate cancer, J. Control. Release 375 (2024) 767-775.

[34] O. Sartor, J. de Bono, K.N. Chi, K. Fizazi, K. Herrmann, K. Rahbar, S.T. Tagawa, L.T. Nordquist, N. Vaishampayan, G. El-Haddad, C.H. Park, T.M. Beer, A. Armour, W.J. Pérez-Contreras, M. DeSilvio, E. Kpamegan, G. Gericke, R.A. Messmann, M.J. Morris, B.J. Krause, Lutetium-177–PSMA-617 for Metastatic Castration-Resistant Prostate Cancer, N. Engl. J. Med. 385(12) (2021) 1091-1103.

[35] A. Mullard, FDA approves first PSMA-targeted radiopharmaceutical, Nature Reviews Drug Discovery 21(5) (2022) 327-327.

[36] H. Cabral, Y. Matsumoto, K. Mizuno, Q. Chen, M. Murakami, M. Kimura, Y. Terada, M.R. Kano, K. Miyazono, M. Uesaka, N. Nishiyama, K. Kataoka, Accumulation of sub-100 nm polymeric micelles in poorly permeable tumours depends on size, Nat. Nanotechnol. 6(12) (2011) 815-823.

[37] J. Wang, W. Mao, L.L. Lock, J. Tang, M. Sui, W. Sun, H. Cui, D. Xu, Y. Shen, The Role of Micelle Size in Tumor Accumulation, Penetration, and Treatment, ACS Nano 9(7) (2015) 7195-206.

[38] T.B. Toh, J.J. Lim, E.K.-H. Chow, Epigenetics in cancer stem cells, Mol. Cancer 16(1) (2017) 29.

[39] L. Zhao, X. Zhang, X. Wang, X. Guan, W. Zhang, J. Ma, Recent advances in selective photothermal therapy of tumor, J. Nanobiotechnology 19(1) (2021) 335.

[40] Y. Li, H.A. Rogoff, S. Keates, Y. Gao, S. Murikipudi, K. Mikule, D. Leggett, W. Li, A.B. Pardee, C.J. Li, Suppression of cancer relapse and metastasis by inhibiting cancer stemness, Proc. Natl. Acad. Sci. U. S. A. 112(6) (2015) 1839-1844.

[41] D. Han, T. Yu, N. Dong, B. Wang, F. Sun, D. Jiang, Napabucasin, a novel STAT3 inhibitor suppresses proliferation, invasion and stemness of glioblastoma cells, J. Exp. Clin. Cancer Res. 38(1) (2019) 289.

[42] J. Czernin, K. Current, C.E. Mona, L. Nyiranshuti, F. Hikmat, C.G. Radu, K. Lückerath, Immune-Checkpoint Blockade Enhances 225Ac-PSMA617 Efficacy in a Mouse Model of Prostate Cancer, J. Nucl. Med. 62(2) (2021) 228-231.

[43] S. Tohme, R.L. Simmons, A. Tsung, Surgery for Cancer: A Trigger for Metastases, Cancer Res. 77(7) (2017) 1548-1552.

[44] M. Alieva, J. van Rheenen, M.L.D. Broekman, Potential impact of invasive surgical procedures on primary tumor growth and metastasis, Clin. Exp. Metastasis 35(4) (2018) 319-331.

[45] F.G. Giancotti, Mechanisms governing metastatic dormancy and reactivation, Cell 155(4) (2013) 750-764.

[46] G. Grillo, T. Keshavarzian, S. Linder, C. Arlidge, L. Mout, A. Nand, M. Teng, A. Qamra, S. Zhou, K.J. Kron, A. Murison, J.R. Hawley, M. Fraser, T.H. van der Kwast, G.V. Raj, H.H. He, W. Zwart, M. Lupien, Transposable Elements Are Co-opted as Oncogenic Regulatory Elements by Lineage-Specific Transcription Factors in Prostate Cancer, Cancer Discov. 13(11) (2023) 2470-2487.

Graphical abstract